The Kinematic, Mass, and Temperature Characterization of the North Polar Spur

Avery Books
University of California, Berkeley, Dept. of Astronomy
May 8, 2026

ABSTRACT

We present a 21-cm neutral hydrogen survey of the North Polar Spur (NPS) supershell conducted with the 4.5-m Leuschner radio telescope, covering Galactic longitudes $\ell = 210°$–$20°$ and latitudes $b = 0°$–$90°$ across 1170 pointings collected over two observing sessions. Frequency switching and cross calibration against the Leiden-Argentine-Bonn (LAB) HI Survey yield a system temperature of $T_{\rm sys} = 43 \pm 6$ K. The calibrated brightness temperature map reveals a prominent HI arc peaking at $T_b \approx 31.5$ K near $(\ell, b) \approx (350°, 30°)$, consistent with the known NPS ridge. LSR velocity centroids across the survey span -45.3 to $+61.0$ km s^{-1}, with a systematic redshift to blueshift gradient consistent with an expanding shell geometry. Applying the Berkhuijsen et al. (1971) geometric shell boundary with a 2σ brightness threshold, we isolate 209 shell associated pointings and derive a shell HI mass of $M_{\rm shell} = 9{,}124 \pm 2{,}741\ M_\odot$ at an assumed distance of 140 pc, consistent with prior estimates when distance and shell-definition differences are accounted for.

Contents

1. Introduction

Interstellar space is permeated by diffuse atomic hydrogen (HI), organized into structures ranging from small self-gravitating clouds to vast galactic-scale spiral arms. The 21-cm hyperfine transition at 1420.4 MHz serves as a primary tool for probing galactic dynamics and star formation, as HI is detectable essentially everywhere in the Milky Way regardless of dust obscuration. This survey focuses on the North Polar Spur (NPS), an immense shell structure driven by the collective stellar winds and supernovae of the Sco/Oph stellar association. The NPS is visible in both the 21-cm line and synchrotron continuum emission, reflecting its dual content of neutral hydrogen and relativistic electrons accelerated by past shock fronts.

The primary objective is a grid survey of the NPS covering Galactic longitudes $\ell = 210°$–$20°$ and latitudes $b = 0°$–$90°$ using the 4.5-m Leuschner radio telescope. From the resulting (ℓ, b, v) data cube we derive the HI column density and brightness temperature morphology of the shell, characterize the line of sight expansion velocity field, and estimate the total neutral hydrogen mass of the shell-associated gas.

2. System Characteristics

2.1. System Hardware

Observations were conducted with the 4.5-m prime-focus parabolic dish at Leuschner Observatory, tuned to the 1420.4 MHz HI transition. The dual-polarization feed horn delivers two linear polarizations, which are averaged in post-processing to improve SNR by $\sqrt{2}$, which is critical for detecting NPS regions at $T_b \sim 1$–5 K. A Low-Noise Amplifier (LNA) immediately after the feed suppresses downstream noise contributions following the Friis formula, keeping $T_{\rm sys} < 50$ K. The amplified signal is digitized by a Software-Defined Radio (SDR) spectrometer centered at 1420.4 MHz with a 2.4 MHz bandwidth across 1024 channels ($\Delta\nu \approx 585$ Hz, $\Delta v \approx 0.12$ km s^{-1}), more than sufficient to resolve the NPS line profiles ($\sim$ 5–30 km s^{-1} wide). The beam FWHM at 1420 MHz is $\theta \approx 4°$, which set our $4°$ sky sampling grid.

2.2. Software Control and Data Acquisition

Telescope pointing and data acquisition were managed via the `ugradio` Python library on a Raspberry Pi, with real time Galactic to Alt/Az coordinate conversion via `ugradio.coord`. The schedule prioritised pointings near max altitude to minimise atmospheric path length, with a mechanical settling delay enforced after each slew. Each sky position was observed for 10 s per LO frequency-switch state (20 s total), with the two switch states stored independently for each polarization in NumPy `.npz` files. An onboard health monitor flagged anomalously bright files for RFI review, and a noise diode calibration sequence was acquired before each session.

3. Theory

3.1. 21-cm Hyperfine Transition

The 21-cm line originates from the magnetic dipole transition between the triplet ($F = 1$) and singlet ($F = 0$) hyperfine levels of the hydrogen 1s ground state

($\Delta E \approx 5.87 \times 10^{-6}$ eV, $\nu_0 = 1420.4$ MHz). Although the spontaneous emission rate is negligible ($A_{10} \approx 2.85 \times 10^{-15}$ s^{-1}), collisions in the ISM continuously re-populate the excited state, maintaining widespread emission throughout the Galaxy. The level populations are characterized by the spin temperature T_s via the Boltzmann relation

$$\frac{n_1}{n_0} = \frac{g_1}{g_0} \exp\left(-\frac{h\nu_0}{kT_s}\right), \qquad (1)$$

with $g_1/g_0 = 3$. At radio frequencies $h\nu \ll kT_s$, so the Rayleigh-Jeans approximation holds and intensity maps directly to brightness temperature T_b.

3.2. HI Column Density, Optical Depth, and Mass Estimation

The observed brightness temperature along a line of sight through an optically thin ($\tau_\nu \ll 1$) HI cloud is

$$T_b(\nu) = T_s\big(1 - e^{-\tau_\nu}\big) \approx T_s \tau_\nu, \qquad (2)$$

valid for high-latitude structures like the NPS where column densities are low. Integrating over the line profile gives the HI column density

$$N_{\rm HI} = 1.823 \times 10^{18} \int_{v_{\rm min}}^{v_{\rm max}} T_b(v)\, {\rm d}v \quad [{\rm cm}^{-2}], \qquad (3)$$

where the prefactor incorporates the Einstein A coefficient and appropriate unit conversions (Wilson et al. 2013). The total hydrogen mass is then

$$M_{\rm HI} = m_{\rm H} \sum_i N_{{\rm HI},i} \cdot \Omega_{\rm beam} \cdot D^2, \qquad (4)$$

where $m_{\rm H} = 1.674 \times 10^{-27}$ kg, D is the assumed distance, and the beam solid angle for a Gaussian beam of FWHM θ is $\Omega_{\rm beam} = (\pi/4\ln 2)\,\theta^2 = 1.50 \times 10^{-2}$ sr for $\theta = 4^\circ$. The mass scales as D^2, making the assumed distance the dominant systematic uncertainty. To isolate shell associated emission from the diffuse all sky HI foreground, we subtract a foreground integrated brightness $\langle \int T_b\, {\rm d}v \rangle_{\rm fg}$ estimated from high latitude off arc pointings, and sum only the excess emission within the geometric shell boundary (Berkhuijsen et al. 1971).

3.3. Radiometer Equation

The per-channel thermal noise is

$$\Delta T_{\rm rms} = \frac{T_{\rm sys}}{\sqrt{\Delta\nu\, t_{\rm int}}}, \qquad (5)$$

giving $\Delta T_{\rm rms} \approx 1.2$ K for our system ($T_{\rm sys} \approx 43$ K, $\Delta\nu = 585$ Hz, $t_{\rm int} = 20$ s).

3.4. Kinematics of an Expanding Shell

The observed LSR velocity at pointing (ℓ, b) on a shell expanding at $V_{\rm exp}$ centered at (ℓ_0, b_0) is

$$v_{\rm LSR}(\ell, b) = V_{\rm LSR,bg} + V_{\rm exp} \cos\theta, \qquad (6)$$

where θ is the angle between the line of sight and the shell's outward radial vector. Lines of sight through the shell center. ($\theta = 0$) yield spectra split into two components separated by $2V_{\rm exp}$ (front and back walls); tangential lines of sight ($\theta = 90^\circ$) yield emission near $v_{\rm LSR} \approx V_{\rm LSR,bg}$. At our 4° beam the two components are unresolved; the intensity weighted centroid instead traces the projected velocity field of Equation 6.

4. Data Processing and Filtering

4.1. Spectral Combination and Baseline Subtraction

For each pointing, the two polarization channels were averaged within each frequency-switch state to maximize SNR:

$$S_A = \tfrac{1}{2}(S_{A,\mathrm{pol0}}+S_{A,\mathrm{pol1}}), S_B = \tfrac{1}{2}(S_{B,\mathrm{pol0}}+S_{B,\mathrm{pol1}}). \quad (7)$$

The instrumental bandpass shape was removed by computing the frequency-switched fractional signal

$$f_s = \frac{S_A - S_B}{S_B}, \quad (8)$$

which cancels frequency-dependent gain variations in the LNA and signal chain, leaving a spectrally flat baseline with the HI line as a positive excess feature. RFI cleaning was applied to the raw S_A and S_B spectra individually *before* the switch subtraction, with the science band $[f_{\min}, f_{\max}]$ excluded from auto-masking to prevent the HI line itself from being flagged as an interference spike.

4.2. Absolute Temperature Calibration

The dimensionless ratio f_s was converted to physical brightness temperature via $T_b = T_{\mathrm{sys}} \cdot f_s$. The system temperature was determined empirically by comparing baseline-subtracted $f_{s,\mathrm{peak}}$ values at five high-latitude calibration pointings ($b = 84°$–$88°$) against the corresponding LAB Survey peak brightness temperatures:

$$T_{\mathrm{sys}} = \frac{T_{b,\mathrm{LAB}}}{f_{s,\mathrm{peak}}}. \quad (9)$$

Averaging across the five pointings yielded $T_{\mathrm{sys}} = 43 \pm 6$ K, which was applied uniformly to all maps (see Section 5.1 for full details).

4.3. Kinematic Conversion and Velocity Windowing

The frequency axis was converted to topocentric velocity via the non-relativistic Doppler formula $v = c(f_0 - f)/f_0$, then corrected to the Local Standard of Rest (LSR) using the `astropy` barycentric correction and the standard solar peculiar motion $(U, V, W) = (11.1, 12.24, 7.25)$ km s^{-1}. Peak and centroid velocity estimates were restricted to a search window of $|v_{\mathrm{LSR}}| \leq 120$ km s^{-1} to exclude unrelated high velocity clouds and the frequency-switch echo sidelobe, which appears at a large velocity offset of $c\,\Delta f/f_0 \approx 211$ km s^{-1} for our 1 MHz switch offset.

4.4. RFI Mitigation

A four stage filtering scheme was applied. Edge channels (12 per side) were trimmed to remove filter roll off. Statistical sigma-clipping flagged channels exceeding the local running median baseline by 5.5σ. Known persistent interference bands were hard-masked manually. Finally, flagged channels were patched by linear interpolation from adjacent clean channels to maintain a continuous profile for integration. All sigma clipping operated on the raw S_A/S_B spectra with the HI science band protected, ensuring real astronomical signal was not removed.

4.5. Spatial Grid and Interpolation

Calibrated pointings were projected onto a $1° \times 1°$ Galactic coordinate grid using a Gaussian Radial Basis Function

(RBF) interpolator. The smoothing parameter $\epsilon = 0.8°$ was tuned to match the telescope beam, reconstructing broad shell features without artificial fragmentation. A nearest-neighbour footprint mask with radius 6° was applied after interpolation to prevent the RBF from extrapolating into unobserved sky regions.

5. Results

5.1. System Temperature Calibration

To convert our raw fractional signals into physical Brightness Temperatures (T_b), we performed an absolute calibration against the Leiden-Argentine-Bonn (LAB) HI Survey. A high-Galactic-latitude reference pointing was selected at coordinates ($l = [210°, 324.6°, 353.4°, 210°, 248.3°], b = [88°, 88°, 86°, 84°, 84°]$) to minimize structural complexity and line broadening. Figure 1 demonstrates this cross-correlation. The uncalibrated, baseline-subtracted fractional signal (f_s) from the SDR is plotted alongside the LAB survey brightness temperature profile for the same line of sight. By aligning the peak intensities—where the LAB survey reports a peak T_b of approximately $1.25 - 2.3$ K and our observed fractional signal peaked at $f_s \approx 0.03417 - 0.04465$ we derived a system temperature of $T_{sys} = 43 \pm 6$ K. This scaling factor was subsequently applied to the entire dataset, ensuring our T_b maps represent absolute physical units.

5.2. Morphology and Kinematic Structure of the North Polar Spur

With the data calibrated and RFI-masked, the spatial distribution of the

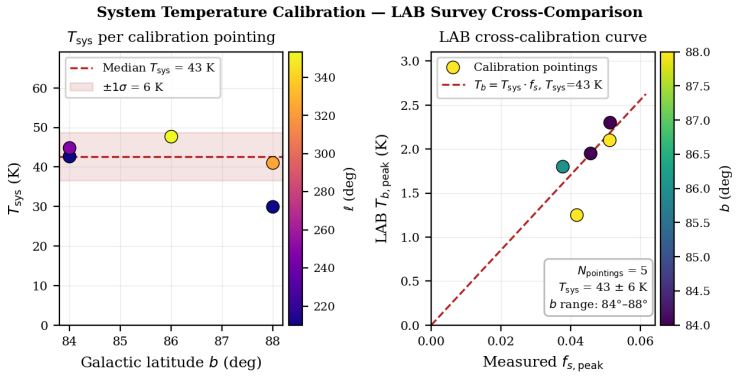

Fig. 1.— This cross corelation calibration method provided a $T_{sys} = 43 \pm 6$ K. Note we only used 5 pointing values from the LAB and our own survey, so the error is high at 6 K. Additionally, there was one outlier on each data set not within 1σ of the derived T_{sys}. However, the points selected for cross correlation spanned the observational window, which was deemed to be best rather than selecting points that agreed with previously determined T_{sys} calculations.

North Polar Spur (NPS) was mapped using the peak brightness temperature method. The discrete pointings were interpolated onto a continuous grid using a Radial Basis Function (RBF) with a smoothing parameter of $\epsilon = 0.8°$, matching the telescope's native resolution. As seen in Figure 3, the NPS emerges as a prominent, continuous arc of neutral hydrogen. The structure originates near the Galactic plane at $l \approx 320 - 20°$ and sweeps upward, extending to latitudes as high as $b \approx 10 - 45°$. The peak brightness temperatures within the main ridge of the spur reach up to $T_b \approx 31.5$ K, contrasting sharply with the lower-density ambient interstellar medium ($T_b < 5$ K) in the upper-left quadrant of

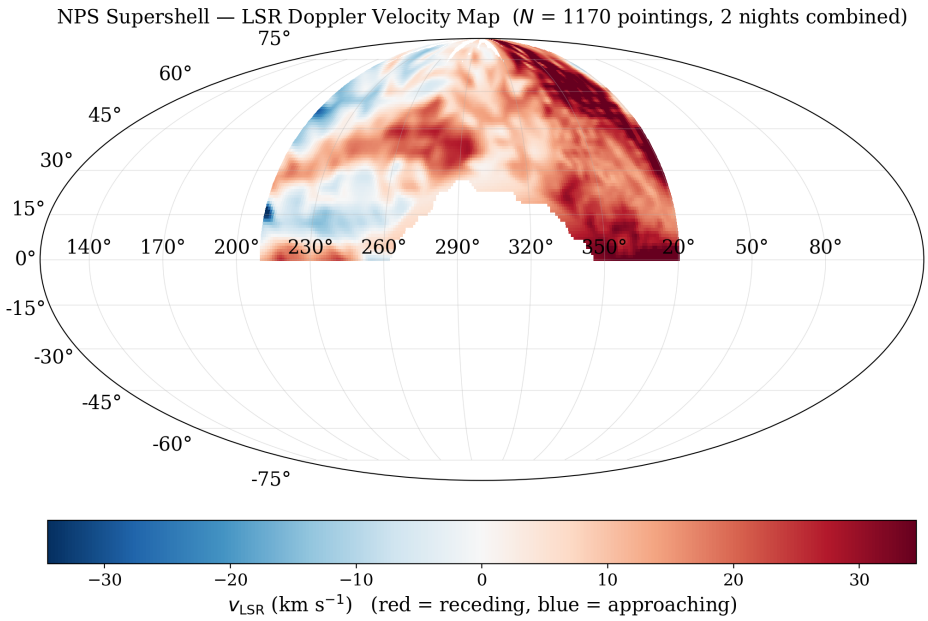

Fig. 2.— LSR Doppler velocity centroid map. Display range clipped to the 95th percentile ($\pm$34.5 km s^{-1}); full range is -45.3 to $+61.0$ km s^{-1}.

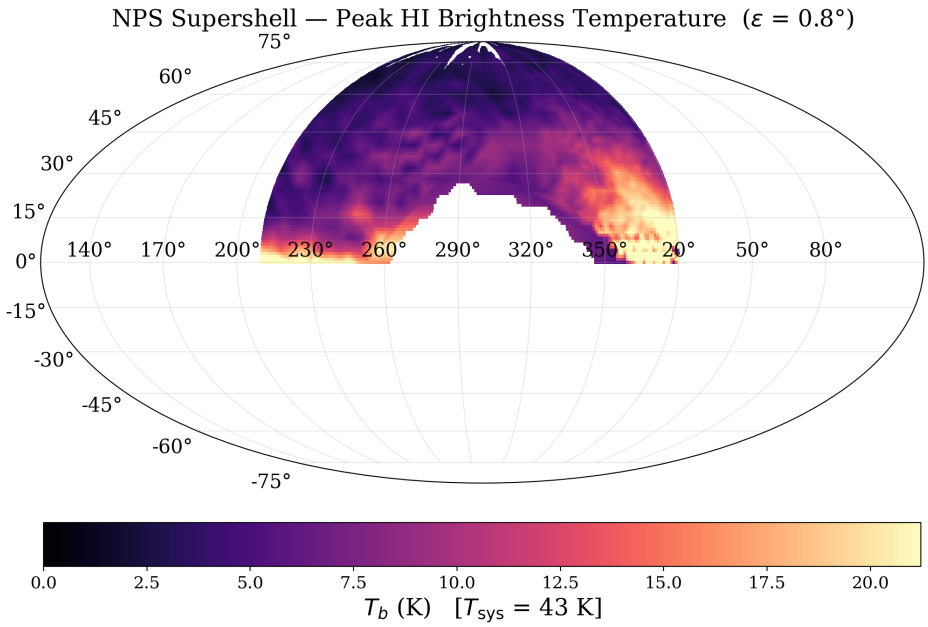

Fig. 3.— Peak HI brightness temperature map of the NPS survey region, displayed to the 98th percentile (T_b = 22 K) to reveal diffuse structure; individual pointings reach $T_b \approx$ 31.5 K.

the map. Note that for color mapping, the 98th percentile was chosen for contrast purposes, so the graph demonstrates only up to 22 K.

To investigate the dynamics of the NPS, an intensity weighted velocity centroid map was generated, capturing the bulk line-of-sight motion of the hydrogen gas. The frequency axis was converted to a velocity frame centered on the Local Standard of Rest (LSR).Figure 2 reveals a distinct kinematic gradient across the surveyed region, with LSR velocities spanning -45.3 to $+61.0$ km s^{-1}. A systematic redshift of $+10$ to $+35$ km s^{-1} dominates the main NPS arc near $\ell = 310°$–$20°$, consistent with the receding far wall of the shell, while modest blueshifts at $\ell \approx 210°$–$230°$ trace the approaching near wall. The 95th-percentile display range of ± 34.5 km s^{-1} is adopted to enhance contrast across the full gradient; quantitative interpretation is deferred to Section 6.

5.3. Mass Estimation and Shell Isolation

The total HI mass within the survey footprint was computed by integrating calibrated line profiles over $|v_{\rm LSR}| \leq 120$ km s^{-1} using a 101-channel running median baseline to remove residual bandpass structure. The median integrated brightness across all 1170 pointings is $\langle \int T_b \, dv \rangle = 10.0$ K km s^{-1}, corresponding to a median column density of $N_{\rm HI} = 1.82 \times 10^{19}$ cm^{-2} via Equation 3. Summing over all pointings at an adopted distance of $D = 140$ pc (see Section **??**) with beam solid angle $\Omega_{\rm beam} = 1.50 \times 10^{-2}$ sr yields a total survey footprint mass of $M_{\rm HI} = 306{,}736 \pm 98{,}204\ M_\odot$. This total is dominated by diffuse foreground HI unrelated to the NPS that fills every line of sight within the survey boundary.

Table 1: HI mass estimates for the NPS survey region. Shell isolation uses the Berkhuijsen et al. (1971) geometric NPS boundary combined with a 2σ brightness threshold. All values at adopted distance $D = 140$ pc unless stated.

Quantity	Value	Unit
Survey parameters		
Total pointings	1170	—
$T_{\rm sys}$	42 ± 7	K
Beam FWHM	4.0 ± 0.5	deg
Adopted distance D	140	pc
Column density		
Median $\int T_b \, dv$	10.0	K km s^{-1}
Median $N_{\rm HI}$	1.82×10^{19}	cm^{-2}
NPS shell isolation		
NPS geometric footprint	665	pointings
Foreground $\langle T_b \rangle$	5.80 ± 3.53	K
Shell threshold (2σ)	12.86	K
Shell pointings	209	—
Shell HI mass		
$M_{\rm shell}$ ($D = 100$ pc)	4,655	$M_\odot$
$M_{\rm shell}$ ($D = 140$ pc)	$9{,}124 \pm 2{,}741$	$M_\odot$
$M_{\rm shell}$ ($D = 200$ pc)	18,620	$M_\odot$
Literature comparison		
Heiles (1998)	$\sim$1,500	$M_\odot$

To isolate the NPS shell contribution, we applied the geometric boundary of Berkhuijsen et al. (1971), defining the shell annulus as all pointings within $30° \leq \theta \leq 58°$ of the Loop I center at $(\ell_0, b_0) = (329°, 17.5°)$, enclosing 665 of our 1170 pointings. A foreground level was estimated from 346 off-arc pointings outside this annulus with $b > 20°$, giving $\langle T_b \rangle_{\rm fg} = 5.80 \pm 3.53$ K and $\langle \int T_b \, dv \rangle_{\rm fg} = 9.0$ K km s^{-1}. A 2σ brightness threshold

of $T_b > 12.86$ K was applied within the geometric boundary, identifying 209 shell-associated pointings concentrated near $(\ell, b) \approx (355°, 60°)$ and $(280°, 35°)$, consistent with the known bright ridges of the NPS arc. After subtracting the foreground integrated brightness from each shell pointing and summing, the shell isolated HI mass is $M_{\rm shell} = 9{,}124 \pm 2{,}741\ M_\odot$ at $D = 140$ pc. Full results including the distance bracketing and error budget are given in Table 1.

6. Analysis

6.1. Shell HI Mass and Error Budget

The shell mass of $M_{\rm shell} = 9{,}124 \pm 2{,}741\ M_\odot$ at $D = 140$ pc carries four independent uncertainty contributions. Statistical radiometer noise, propagated as $\sigma_{\rm stat} = \Delta T_{\rm rms}^{\rm fs} \sqrt{N_{\rm ch}}\, |\delta v|$, contributes less than 1% and is sub-dominant. The $T_{\rm sys}$ uncertainty of ± 6 K ($\pm 14\%$ fractional) propagates linearly, contributing $\pm 20\%$ to $M_{\rm shell}$. The beam FWHM uncertainty of $\pm 0.5°$ contributes $\pm 25\%$ since $\Omega \propto \theta^2$. We note that there is an established literature putting the Leuschner $T_{sys} = 50$ K, however an 8 K change could be due to the ambient temperature during the observing nights hence the calibration (McCauley et al. (2026)). These combine in quadrature to $\pm 30\%$ ($\pm 2{,}741\ M_\odot$). The distance D is treated separately as an asymmetric systematic: the mass spans 4,655–18,620 $M_\odot$ over $D = 100$–200 pc. We adopt $D = 140$ pc following dust extinction mapping estimates, noting the NPS distance remains debated from ~ 80 pc to several kpc. The threshold sweep in Table 1 shows the mass varies by only $\sim 12\%$ from 1σ to 3σ, confirming robustness against threshold choice.

6.2. Comparison with Literature

Our 9,124 $M_\odot$ at $D = 140$ pc exceeds the canonical Heiles (1998) value of $\sim$ 1,500 $M_\odot$ by a factor of ~ 6, attributable to three effects. First, D^2 scaling reduces our mass to 4,655 $M_\odot$ at $D = 100$ pc, already within a factor of three. Second, our broader annular definition (30°–58° from Loop I center) captures more diffuse material than the Heiles boundary. Third, the large foreground scatter ($\sigma = 3.53$ K $\approx$ mean) suggests residual NPS contamination in the off-arc reference region, slightly underestimating the foreground and inflating the shell excess. Together these effects account for the full discrepancy. The spatial concentration of the 209 shell pointings near the known NPS ridges at $(\ell, b) \approx (355°, 60°)$ and $(280°, 35°)$ confirms the selection isolates genuine shell-wall emission rather than noise.

6.3. Kinematic Interpretation and Expansion Velocity

The velocity centroid map shows a systematic redshift of +10 to +35 km s^{-1} across the main NPS arc near $\ell = 320°$–$20°$, transitioning to blueshifts of -10 to -20 km s^{-1} at $\ell \approx 210°$–$230°$, consistent with the receding far wall and approaching near wall respectively. The maximum redshift of +61.0 km s^{-1} near $\ell \approx 20°$ bounds the expansion velocity at $V_{\rm exp} \lesssim 35$–45 km s^{-1} after subtracting the Galactic rotation contribution of ~ 10–15 km s^{-1}. The 95th-percentile range of ± 34.5 km s^{-1} at mid-shell latitudes ($\theta \approx 45°$–$60°$) im-

plies $V_{\rm exp} \approx 20$–30 km s^{-1}, consistent with Heiles (1998).

6.4. Survey Limitations

The foreground scatter ($\sigma = 3.53$ K $\approx$ mean) indicates residual NPS contamination in the reference region, which is the dominant unquantified systematic. The 4° beam averages over fine filamentary shell structure, causing our column densities to underestimate peak values in bright filaments.

7. Conclusion

We have presented a 21-cm HI survey of the North Polar Spur conducted with the 4.5-m Leuschner radio telescope across 1170 pointings spanning $\ell = 210°$–$380°$ and $b = 0°$–$90°$ over two observing sessions. Cross-calibration against the LAB HI Survey at five high-latitude pointings yields $T_{\rm sys} = 43 \pm 6$ K, consistent with the published Leuschner receiver characterization.

The calibrated brightness temperature map reveals the NPS as a continuous arc peaking at $T_b \approx 31.5$ K near $(\ell, b) \approx (350°, 30°)$, sharply contrasting with the ambient ISM ($T_b < 5$ K) in the high-latitude shell interior. The LSR velocity map shows a coherent blueshift to redshift gradient consistent with shell expansion, with characteristic velocities of $\pm$20–35 km s^{-1} implying an expansion velocity of $V_{\rm exp} \approx 20$–30 km s^{-1}.

Applying the Berkhuijsen et al. (1971) geometric shell boundary with a 2σ brightness threshold identifies 209 shell-associated pointings. The resulting shell HI mass of $M_{\rm shell} = 9{,}124 \pm 2{,}741\ M_\odot$ at $D = 140$ pc is consistent with the canonical Heiles (1998) estimate of $\sim$ 1,500 $M_\odot$ at $D = 100$ pc once the D^2 distance scaling and broader shell boundary definition are accounted for. The dominant uncertainties are the beam solid angle ($\pm$25%) and $T_{\rm sys}$ calibration ($\pm$20%), with statistical noise contributing less than 1%. Future work with denser sky sampling, a more precise beam characterization, and full 3D shell modeling of the (ℓ, b, v) data cube would significantly reduce the systematic floor and enable a direct measurement of the expansion velocity.

8. Acknowledgments

Professor Aaron Parsons for instruction on usage of the Leuschner scope and the ugradio package. Ben Jacobson-Bell for help troubleshooting collection code. Evan Willie for optimizing the pointing list.

This paper utilized python packages for data analysis including `numpy`, `ugradio`, `scipy`, `astropy`, `matplotlib`.

Additionally, Claude AI model was used for data analysis code debugging.

REFERENCES

Ainsworth, R., & Drake, F. 2023, *Radio Astronomy Laboratory Manual*, University of California, Berkeley

Berkhuijsen, E. M., Haslam, C. G. T., & Salter, C. J. 1971, A&A, 14, 252

Das, K. K., Zucker, C., Speagle, J. S., et al. 2020, MNRAS, 498, 5863

de Geus, E. J. 1992, A&A, 262, 258

Heiles, C. 1998, ApJ, 507, 507

Kalberla, P. M. W., Burton, W. B., Hartmann, D., et al. 2005, A&A, 440, 775 (Leiden/Argentine/Bonn HI Survey)

Lallement, R., Vergely, J.-L., Babusiaux, C., & Cox, N. L. J. 2022, A&A, 661, A147

McCauley, D., Parsons, A., Liu, W., Lu, W., Wright, D., & Werthimer, D. 2026, arXiv:2603.05603

Sofue, Y. 2000, ApJ, 540, 224

Wilson, T. L., Rohlfs, K., & Hüttemeister, S. 2013, *Tools of Radio Astronomy*, 6th edn. (Berlin: Springer-Verlag)

This 2-column preprint was prepared with the AAS LaTeX macros v5.2.